Carbon outgassing in the Antarctic Circumpolar Current is supported by Ekman transport from the sea ice zone in an observation-based seasonal mixed-layer budget

Jade Sauvé[1], Alison R. Gray[1], Channing J. Prend[1,2], Seth M. Bushinsky[3],Stephen C. Riser[1]

[1]School of Oceanography, University of Washington, Seattle, WA, USA
[2]Environmental Science and Engineering, California Institute of Technology, Pasadena, CA, USA
[3]Department of Oceanography, School of Ocean and Earth Science and Technology, University of Hawaii at Manoa, HI, USA

Key Points:

- We build a Southern Ocean observation-based dissolved inorganic carbon (DIC) budget with circumpolar resolution and a full seasonal cycle.
- Biological activity and circulation dominate the seasonal variations in mixed layer DIC fluxes.
- Wind-driven transport from the seasonal ice zone contributes to carbon outgassing in the Antarctic Circumpolar Current.

Corresponding author: Jade Sauvé, `jsauve@uw.edu`

Abstract

Despite its importance for the global cycling of carbon, there are still large gaps in our understanding of the processes driving annual and seasonal carbon fluxes in the high-latitude Southern Ocean. This is due in part to an historical paucity of observations in this remote, turbulent, and seasonally ice-covered region. Here, we use autonomous biogeochemical float data spanning 6 full seasonal cycles and with circumpolar coverage of the Southern Ocean, complemented by atmospheric reanalysis, to construct a monthly mixed layer budget of dissolved inorganic carbon (DIC). We investigate the processes that determine the annual mean and seasonal cycle of DIC fluxes in two different frontal zones of the Antarctic Circumpolar Current (ACC)—the Sea Ice Zone (SIZ) and Antarctic Southern Zone (ASZ). We find that, annually, mixing with carbon-rich waters at the base of the mixed layer supplies DIC which is then, in the ASZ, either used for net biological production or outgassed to the atmosphere. In contrast, in the SIZ, where carbon outgassing and the biological pump are weaker, the surplus of DIC is instead advected northward to the ASZ. In other words, carbon outgassing in the southern ACC, which has been attributed to remineralized carbon from deep water upwelled in the ACC, is also due to the wind-driven transport of DIC from the SIZ. These results stem from the first observation-based carbon budget of the circumpolar Southern Ocean and thus provide a useful benchmark to evaluate climate models, which have significant biases in this region.

Plain Language Summary

The ocean surrounding the frozen continent of Antarctica plays an important role in the global cycling of carbon and is important for the climate of our planet. Despite it's importance, there are gaps in our knowledge due to the difficulties involved in collecting data from a remote, seasonally ice-covered ocean. In this study, we use year-round data collected by autonomous instruments that can even measure under sea ice. We build a budget of carbon in the surface layer of the ocean, quantifying the different sources and sinks of inorganic carbon. We find that carbon mostly enters the surface layer through mixing with carbon-rich waters below. In the more stormy, northern part of our study area, this carbon is then either consumed by photosynthesis in the ocean or it is transferred to the atmosphere. In the southernmost region, biological activity and gas transfer at the ocean-atmosphere interface is hindered by the presence of sea ice and the surplus of carbon is instead transferred north by wind-driven circulation. Our results show that year-round measurements of carbon are necessary to understand carbon cycling in the region and we provide a useful product to compare to global simulations of the Earth system.

1 Introduction

The Southern Ocean plays a significant role in the global carbon cycle. Around 40% of oceanic uptake of anthropogenic carbon dioxide (CO_2) occurs in the waters south of 35°S (DeVries, 2014). Ekman divergence driven by strong westerly winds leads to a superposition of upwelling and downwelling of natural and anthropogenic carbon, respectively. Consequently, the Southern Ocean is a strong CO_2 sink between 35-55°S, although the picture is not as clear at higher latitudes (Gruber et al., 2019). Historically, observations from this remote region have been strongly biased towards summer and limited spatially, particularly in the seasonally ice-covered areas. Data from autonomous biogeochemical floats deployed by the Southern Ocean Carbon and Climate Observations and Modeling (SOCCOM) project showed a stronger wintertime outgassing of carbon dioxide at high latitudes than expected, leading to a low Southern Ocean annual mean carbon uptake (Gray et al., 2018; Bushinsky et al., 2019). However, another recent study based on airborne measurements found strong Southern Ocean annual mean carbon uptake (Long et al., 2021).

Air-sea carbon fluxes are computed from the difference in CO_2 partial pressure (pCO$_2$) between the atmosphere and the ocean multiplied by a gas transfer velocity and the solubility of CO_2 in the ocean (Gruber et al., 2019; Gray et al., 2018). Since these last two parameters are strictly positive, the sign of the air-sea flux depends solely on the air-sea gradient in pCO$_2$. Spatio-temporal variability in atmospheric CO_2 is small compared to surface ocean pCO$_2$ (Takahashi et al., 1997). Therefore, oceanic pCO$_2$ primarily determines seasonal and regional variations in air-sea carbon fluxes (Takahashi et al., 2002).

The dominant mode of variability for both surface ocean pCO$_2$ and air-sea carbon flux is the seasonal cycle (Gruber et al., 2019). Seasonal changes in ocean pCO$_2$ can be separated into thermal and non-thermal components using the well-known thermal sensitivity of pCO$_2$ (Takahashi et al., 1993). The thermal component is in phase with seasonal temperature changes. Colder waters have a higher dissolved carbon solubility leading to smaller pCO$_2$ for the same amount of dissolved carbon dioxide. The non-thermal component is dominated by changes in dissolved inorganic carbon (DIC), and thus peaks in winter due to respiration and entrainment of subsurface carbon (Takahashi et al., 2002). South of the Sub-Antarctic front, pCO$_2$ seasonality is driven primarily by the non-thermal component (Gruber et al., 2019; Prend et al., 2022). Therefore, surface DIC variability is central to understanding high-latitude Southern Ocean air-sea carbon fluxes. Furthermore, it is useful to quantify the processes that alter mixed-layer DIC concentration in order to understand air-sea carbon flux variations. A range of tracer budgets have been used for this purpose across diverse space and time scales.

As the necessary data is more readily available, there have been numerous DIC budgets constructed from model output, including from coupled models (Levy et al., 2013; Dufour et al., 2013; Hauck et al., 2013), idealized models (Bronselaer et al., 2018) and data-assimilating models (Carroll et al., 2022; DeVries, 2014; Rosso et al., 2017). However, these model-based budgets often average the entire ocean south of a given latitude (usually 44°S) and are computed over a fixed depth. These modelling studies show that both biological and physical processes drive DIC variations, but no clear quantitative agreement has been reached about the leading order terms. In our study region, a small number of observation-based DIC budgets have been constructed using mooring data (Yang et al., 2021), shipboard sections (Brown et al., 2015; Jouandet et al., 2008; McNeil & Tilbrook, 2009), autonomous float data (Williams et al., 2018) or a combination of methods (Shadwick et al., 2015; Merlivat et al., 2015). However, the limited number of studies, as well as the different characteristics of the budgets constructed, preclude any specific conclusions aside from the strong seasonality in the processes driving mixed layer DIC variations. Furthermore, no previous study has provided a large-scale view of Southern Ocean DIC fluxes based on year-round and circumpolar observations.

Recognizing the paucity of year-round biogeochemical data in the Southern Ocean, the SOCCOM project began deploying sea ice-enabled autonomous biogeochemical profiling floats in 2014. Since then, a new database has been growing that can be used to shed light on the carbon cycle in this hard-to-reach environment. In this study, we build a monthly mixed layer DIC budget using SOCCOM float data, complemented with atmospheric reanalysis. This framework allows us to investigate the processes that determine the seasonal cycle of carbon fluxes in different regions; namely, the Sea Ice Zone (SIZ) and Antarctic Southern Zone (ASZ), which are delimited by well-known Southern Ocean fronts (Fig. 1 a)). Section 2 covers the datasets used in this study. Section 3 elaborates on the budget framework, Section 4 presents the results on both annual and seasonal scales, and Section 5 discusses the implications of our results.

2 Datasets

2.1 Float Data

In this study, we use in situ data from the December 2020 snapshot of the SOCCOM Project dataset (doi.org/10.6075/J0B27ST5). This snapshot covers the period from January 2014 to December 22, 2020 and contains data from 201 autonomous biogeochemical profiling floats. SOCCOM floats measure temperature (T), pressure (P) and salinity (S) over the top 2000 m of the water column, every 10 days, similar to a typical Argo float. However, they also carry sensors for dissolved oxygen (O_2), nitrate, pH, chlorophyll fluorescence, and optical backscatter. Floats sample unevenly in the vertical, so all profiles are linearly interpolated onto a regular depth axis with 5 m resolution in the upper 500 m, 10 m resolution from 500-1000 m, 50 m resolution from 1000-1500 m, and 100 m resolution from 1500-2000 m. We only consider profiles with good pH data (i.e. where DIC content can be estimated), which leaves us with 7029 profiles from 132 floats, reasonably well spatially distributed in the Southern Ocean (Fig. 1). We separate profiles according to the month and the frontal zone (see section 3.2) and obtain about 100 profiles per category (Fig. 1 b)). We download a delayed-mode quality-controlled snapshot of the SOCCOM data (Maurer et al., 2021) and keep only the data flagged "Good" except for latitude and longitude, where we additionally keep under-ice data labeled "Questionable."

2.2 Other Data

Monthly composites of the ERA5 reanalysis product, covering the period of January 2014 to December 2020, are used to create seasonal cycles of eastward and northward wind stress, sea ice fraction, and evaporation and total precipitation rate (Hersbach et al., 2020). Monthly fields from the Roemmich-Gilson Argo Climatology (RGAC) for the period of January 2014 to December 2020 are used to compute an average monthly climatology of potential temperature (Roemmich & Gilson, 2009). A gridded product of geostrophic velocity updated from Gray and Riser (2014) with improved mapping and additional data points is used in the geostrophic transport calculations (see section 3.3.3). Finally, we use the bathymetry from the ETOPO1 Global Relief Model (Amante & Eakins, 2009).

3 Budget Framework and Analysis Methods

We create monthly mixed layer budgets of carbon and oxygen based on a box model framework. Boxes are defined by concentric circular fronts of the ACC and the maximum sea ice extent, so that averaging over a region is roughly equivalent to applying a zonal average. Consequently, horizontal fluxes of carbon and oxygen need only be defined at the box's northern and southern edges (Fig. 1 a)). Available float data are selected for a particular box (i.e. frontal region) and then averaged for each month, combining all available years to get a climatological seasonal cycle for each frontal zone. We derive the mixed layer budget equation by volume integrating the tracer conservation equation for an arbitrary tracer, X, in this case DIC or O_2. The volume of the box can be converted to the product of the mixed layer depth (h) by the ocean surface area (A) of the box.

$$\int_A \int_{-h(t)}^{0} \left[\frac{\partial(\rho[X])}{\partial t} + \vec{u} \cdot \nabla(\rho[X]) = f_{air-sea} + \kappa_z \frac{\partial^2(\rho[X])}{\partial z^2} \right] dz dA \tag{1}$$

After solving and applying the appropriate assumptions, we obtain the final form of the budget equation (see Section 3.3 and Supplementary Information for details).

$$\frac{\partial(\rho[X]h)}{\partial t} = \rho[X]\big|_{-h} \frac{dh}{dt} - \frac{1}{A} \left[(\rho[X]V_{ek})\big|_N - (\rho[X]V_{ek})\big|_S + (\rho[X]V_{geo})\big|_N - (\rho[X]V_{geo})\big|_S \right] +$$

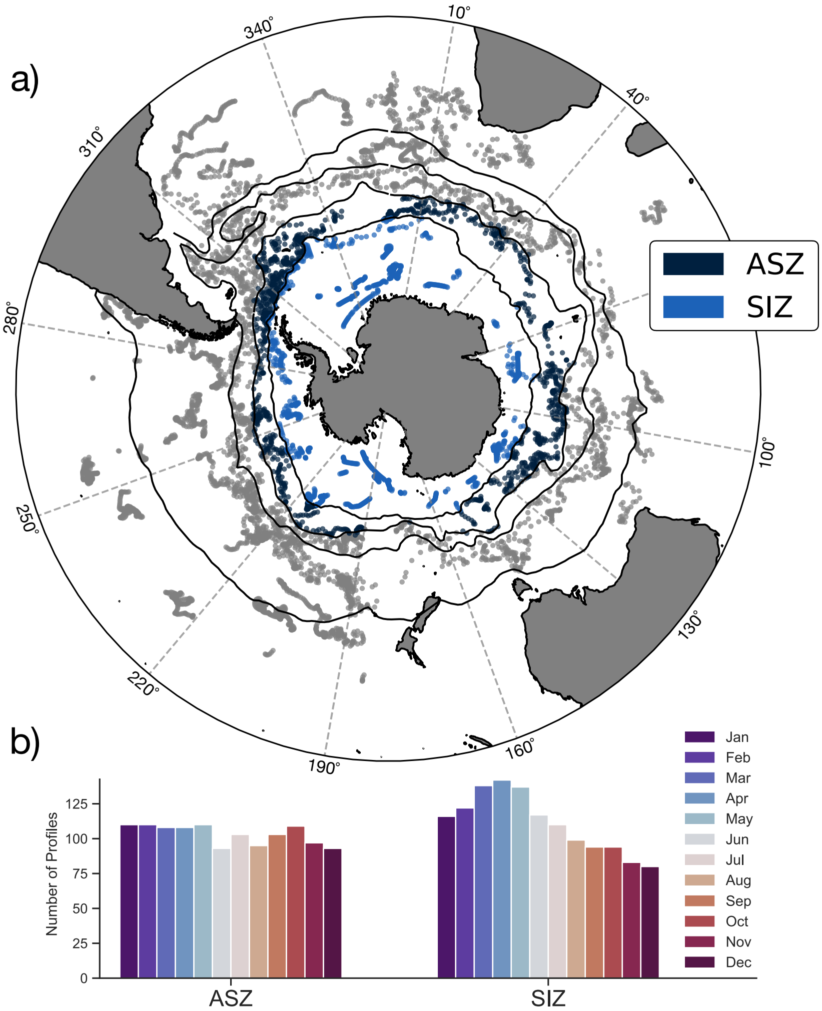

Figure 1. a)Location of available float profiles with good pH data (i.e. where DIC can be estimated), colored by frontal region. b) Number of profiles available for analysis per month and per frontal region (ASZ: Antarctic Southern Zone, SIZ: Sea Ice Zone).

$$\mathrm{w}\rho[X]\big|_{-h} + F_{air-sea} - \kappa\frac{\partial(\rho[X])}{\partial z}\bigg|_{-h} + F_{bio}(2)$$

In this form, we have canceled out the ocean surface area of the frontal region. However, multiplying any term by this area will return units of mol time^{-1}, which properly reflects the fact that our budget tracks the total quantity of DIC in the mixed layer over time. Each term of Eq. 2 represents a different process that can cause an increase or decrease in tracer mixed layer molar concentration (mol m^{-3}). Eq. 2 can be expressed in terms of the different fluxes at play, namely

$$TEND = F_{entrain} + F_{horiz-adv} + F_{vert-adv} + F_{air-sea} + F_{mixing} + F_{bio} \quad (3)$$

In Section 3.3, we give a detailed overview of each term and its derivation.

3.1 Initial Processing of the Float Data

We follow the method used by the SOCCOM project to determine DIC from the float data (Johnson et al., 2017; Wanninkhof et al., 2016). We estimate total alkalinity (TA) by using float-derived T, S, and O_2 as inputs to the LIAR algorithm (Carter et al., 2018). To estimate DIC, we use the CO_2 System Calculator for Python (PyCO2SYS) which requires two carbonate system parameters, TA and in situ pH, as well as measured T, S, and P (Humphreys et al., 2021). We also provide total silicate and total phosphate concentrations estimated using stochiometric ratios of float-derived nitrate concentration. We use the equilibrium constant parameterizations of Lueker et al. (2000) to model carbonic acid dissociation, Dickson (1990) for bisulfate ion dissociation, Perez and Fraga (1987) for hydrogen fluoride dissociation, and Lee et al. (2010) for the boron:salinity relationship to estimate total borate.

We take the quality-controlled float data and average the relevant quantities in the mixed layer. To estimate the mixed layer depth (MLD), we find the absolute salinity and the conservative temperature using the Gibbs Sea-Water Oceanographic Toolbox for Python (McDougall & Barker, 2011). From those, we estimate the in-situ density (ρ) and the potential density anomaly with reference pressure of 0. We then interpolate the potential density anomaly to 0.01 dbar increments and use a density variation threshold of 0.03 kg m^{-3} from a reference pressure of 10 dbar from the surface to identify an approximate pressure for the base of the mixed layer (de Boyer Montégut et al., 2004; Holte & Talley, 2009). Using this mixed layer pressure (MLP) and selecting profiles which have at least one value in the top 30 dbar and at least 2 values in the top 1000 dbar, we fit a curve using a pchip interpolator and find the average concentration in the mixed layer. This averaging is executed for the biogeochemical tracers' molality (concentration of tracer in mol kg^{-1} of seawater) multiplied by ρ to obtain the average mixed layer molar concentration of each variable (mol m^{-3}, called concentration for the remainder of this study). We also find the vertical gradient below the mixed layer by fitting a straight line through the data between the MLP and 20 dbar deeper, finding its slope and converting to depth units by multiplying by $-g\rho 10^{-4}$. We then average the float data monthly and by frontal region, multiplying by h beforehand as the budget equation requires.

3.2 Frontal Regions

To sort profiles by frontal zone, we compute the position of the fronts at monthly resolution by applying the well-known Orsi et al. (1995) criteria to the RGAC monthly climatology of potential temperature (Fig. S1). More specifically, we use the 2°C contour at the minimum potential temperature of the top 200 m for the Polar Front (PF) and the 15% sea ice concentration contour in September for the Sea Ice Front (SIF). For the frontal zones that include coastal waters, we define the area of the zone where waters are at least 1000 m deep. From these two fronts, we define 2 zones, shaped like concentric circles around the continent of Antarctica (Fig.1 a)). The sea ice zone (SIZ) is defined as the region south of the SIF. The Antarctic Southern zone (ASZ) can be found north of the SIF and south of the PF. This is similar to a number of previous papers (Gray et al., 2018; Bushinsky et al., 2019).

3.3 Budget Terms

The following section will provide details about the different terms of the mixed layer budget and their derivation.

3.3.1 Tendency and Entrainment Flux

The left-hand side, or tendency (TEND), of Eq. 2 corresponds to the time rate of change of the tracer concentration (mol m^{-3}) in the box. The entrainment flux is due to the process by which the base of the mixed layer deepens or shoals. During mixed layer deepening, water below the mixed layer is integrated into the surface layer leading to mixed layer volume and tracer content increasing, proportionally to the amount of tracer in the waters just below the base of the mixed layer. During mixed layer shoaling, mixed layer volume decreases and so does the amount of tracer in the mixed layer, proportionally to the mixed layer concentration. Both the TEND and $F_{entrain}$ can be estimated from float-derived molality, h and ρ, using a centered difference calculation. Integrating the first component of Eq. 1 over a time-varying $h(t)$ produces two terms, the tendency term (the rate of change of the total tracer amount) and the entrainment term (proportional to the rate of change of the MLD) (see Supplementary Information for details). The tendency term is given by

$$TEND = \frac{\partial(\rho[X]h)}{\partial t} \tag{4}$$

and the entrainment term is expressed as

$$F_{entrain} = \rho_{-h}[X]_{-h}\frac{dh}{dt} \quad if\ \frac{dh}{dt} > 0 \tag{5}$$

$$F_{entrain} = \rho[X]\frac{dh}{dt} \quad if\ \frac{dh}{dt} < 0 \tag{6}$$

both terms having been divided by the area to be consistent with Eq. 3.

It is important to note that the subtraction of the entrainment flux from the tendency is equivalent to the rate of change of the concentration multiplied by the mixed layer depth. This will be used in the presentation of the results.

$$\frac{\partial(\rho[X]h)}{\partial t} - (\rho[X])_{-h}\frac{dh}{dt} = h\frac{\partial(\rho[X])}{\partial t} \tag{7}$$

3.3.2 Air-Sea Flux

We estimate the air-sea fluxes of carbon using the method from Gray et al. (2018). Using float-measured pH and a float-based estimate of alkalinity, we compute $p\mathrm{CO}_2$ at the surface of the ocean. Then using ground-based atmospheric CO_2 measurements, the air-sea flux of carbon can be estimated using the following equation, where k_g is the gas transfer velocity and k_0 is the solubility of CO_2:

$$f_{air-sea} = k_g k_0 (p\mathrm{CO}_2^{ocn} - p\mathrm{CO}_2^{atm}). \tag{8}$$

Because carbon dioxide is highly soluble in seawater, we do not need to account for the effect of bubble fluxes.

We estimate the oxygen air-sea fluxes following Bushinsky et al. (2017) (updated to March 2020). Contrarily to carbon, the residence time in the mixed layer of oxygen is much faster (on the order of 2 weeks depending on the MLD), and bubble fluxes must be taken into account. The total air-sea flux is thus made up of three components: F_s is the diffusive component, F_c accounts for small bubbles that collapse while under water, and F_p accounts for big bubbles that partly escape the water column. β is the tuning parameter.

$$f_{air-sea} = F_s + \beta F_c + \beta F_p \tag{9}$$

To obtain the form of $F_{air-sea}$ that is consistent with Eq. 3, we compute the air-sea flux at high frequency (6-hourly) and then find the average air-sea flux of tracer per meter squared (mol m^{-2} day^{-1}) for each frontal region.

3.3.3 Advective Flux

The advective fluxes originate from the second term of Eq. 1, which we separate into a horizontal and a vertical component. We consider the horizontal advection crossing the frontal boundaries at the northern and southern edges of the box only. In the Southern Ocean, cross-front (largely meridional) advection at the surface is mostly due to Ekman transport, which is northward due to the strong westerly winds. Additional contributions to the cross-front advection come from the geostrophic flow, which can be decomposed into low-frequency (mean and seasonal cycle) and high-frequency (eddying) components. In the context of this work, we neglect the cross-front advection due to eddies because it has been shown to be more than 50% smaller than the time mean component in the Ekman layer (Dufour et al., 2015). Defining V_{ek} and V_{geo} as the Ekman and geostrophic mass transports, the final form of the horizontal advection term equation, as consistent with Eq. 3, becomes

$$F_{horiz-adv} = -\frac{1}{A}\left[(\rho[X]V_{ek})\big|_N - (\rho[X]V_{ek})\big|_S + (\rho[X]V_{geo})\big|_N - (\rho[X]V_{geo})\big|_S\right] \tag{10}$$

(see Supplementary Information for details). Here, $\rho[X]\big|_N$ ($\rho[X]\big|_S$) corresponds to the tracer concentration of the source water of the horizontal advection at the northern (southern) boundary. This will change depending on the direction of mass flux (northward or southward). For example, Ekman transport in this region is northward. Consequently, we multiply the Ekman mass transport at the northern (southern) boundary of the zone by the concentration of tracer in (just South of) the frontal region (Fig. S4).

We can compute the Ekman mass transport (V_{ek}) using ERA5 wind stress data. We take the monthly averaged wind stress and interpolate the data to each (latitude, longitude) points defining the frontal boundaries. Using both the zonal and the meridional wind stress, we compute the component of the wind stress parallel to each front segment, defined by two (latitude, longitude) points. Taking the along-front wind stress, we convert it to the depth integrated Ekman velocity across the front using the Coriolis equation (Eq. S10). Integrating further zonally around the front, we obtain the Ekman transport across the frontal boundary (m^3 time^{-1}).

The geostrophic mass transport is computed using an updated version of the geostrophic velocity product from (Gray & Riser, 2014). Similarly to the process for Ekman transport, the data is interpolated to front locations and the across-front geostrophic velocity is identified at each segment of the frontal boundaries. This geostrophic velocity is then integrated zonally along the frontal boundary before being integrated further in depth to the mixed layer depth of the zone being considered.

The vertical advection at the base of the mixed layer depends on the vertical velocity at the base of the mixed layer (w_{-h}) as well as on the concentration of tracer ($\rho[X]\big|_{-h}$) in the downwelled or upwelled waters depending on the sign of w_{-h}.

$$F_{vert-adv} = (w\rho[X])\big|_{-h} \tag{11}$$

Vertical velocity is more challenging to determine from satellite products as it is comparatively small. We use a mixed layer mass budget to determine the monthly-mean vertical velocity averaged across each zone. The equation for the mixed layer mass budget is determined by integrating the advection-diffusion equation for density over the mixed layer volume in a process similar to the derivation for the tracer conservation equation. The resulting equation has many of the same terms as the biogeochemical budget equation.

$$\frac{d(A\rho h)}{dt} = F_{entrain} + F_{surface} + F_{horiz-adv} + F_{vert-adv} \tag{12}$$

The rate of change with time of the mass of water in the mixed layer as well as the entrainment flux of water can both be determined from float-derived data following Eq. 7 applied to the density (kg m^{-3}) instead of the concentration of tracer (mol m^{-3}). Similarly, the horizontal mass advection can be determined following Eq. 10. We use ERA5 precipitation, evaporation, and sea ice concentration data to estimate surface fluxes of mass ($F_{surface}$). For the sea ice contribution, we take the centered difference of the sea ice area combined with an estimated seasonal sea ice thickness (Li et al., 2018) to find the rate of change with time of the sea ice volume for each month. Since the mass budget doesn't have biological fluxes or fluxes due to mixing, there is only one unknown, w_{-h}, which we solve for (Fig.S3).

3.3.4 Mixing Flux

Vertical mixing represents multiple processes involving the gradient of tracer concentration between the mixed layer and the waters underlying it. It differs from vertical advection because there is no exchange of mass. It is typically parameterized in terms of a vertical eddy diffusivity (κ_z), which ideally is tuned to observations. The mixing flux term corresponds to the last term of Eq. 1,

$$F_{mixing} = -\kappa_z \frac{\partial(\rho[X])}{\partial z}\bigg|_{-h} \tag{13}$$

(see Supplementary Information for details). There are very few observations of the vertical eddy diffusivity in the Southern Ocean and few observations at the base of the mixed layer. Law et al. (2003) estimate that the mean effective vertical diffusivity is less than 0.3×10^{-4} m^2 s^{-1} in the Antarctic Circumpolar Current (ACC) region (61°S 140°E) using a tracer dispersion experiment. Cronin et al. (2015) used data from moorings, satellites, and Argo floats to construct mixed layer budgets of heat and salt and estimate the residual diffusive flux of heat or salt across the base of the mixed layer. This residual flux implies a vertical eddy diffusivity of 1 to 3×10^{-4} m^2 s^{-1} in summer and spring for an open ocean location in the Northeast Pacific subpolar gyre. Please refer to section 3.4 for details on how we estimate this parameter for the budgets presented here.

3.3.5 Biological Flux

The net contribution of all biological activity to changes in the concentration of tracer in the mixed layer of each zone is represented by the biological flux term (F_{bio}). Also included in this quantity are any non-explicitly represented physical processes. In the following section, we detail the method used to estimate both this term and the unknown eddy diffusivity parameter necessary for the mixing flux.

3.4 Optimization of the Coupled DIC and O_2 Budgets

To find the few parameters that cannot be easily estimated from float or reanalysis data, we define, for each frontal region, a system of 24 non-linear coupled equations (the monthly equations for the DIC and O_2 budgets) with 14 unknowns, where Y_X represents all terms that can be estimated from float or reanalysis data.

$$Y_{DIC} = -\kappa_z \frac{\partial\rho[C]}{dz}\bigg|_{-h} + F_{biology-DIC} \tag{14}$$

$$Y_{O_2} = -\kappa_z \frac{\partial \rho [O_2]}{dz}\bigg|_{-h} + R_{O_2/C} F_{biology-DIC} \tag{15}$$

We assume a single value of eddy diffusivity (κ_z) for all months in a frontal region. We use the respiration quotient (R_{O_2}) to link the biological flux of DIC and O_2 and assume that this ratio doesn't change from month to month in a particular zone. This leaves us with 12 monthly carbon biological fluxes, one value of κ_z and one value of R_{O_2} as the unknowns for each region. Using our system of equations, we construct a cost function that we minimize to determine the missing parameters. We use the Trust Region Reflective algorithm as part of a non-linear problem solver, to which we provide a Jacobian, to find a local minimum of our cost function (Branch et al., 1999).

3.5 Uncertainty estimation

Unlike model budgets which can be closed exactly, our budget framework is based on several observational products, which each have their own uncertainties. Furthermore, we have used an optimization method to find the value of some parameters. As such, the budget has a non-zero residual (Fig.S8 and S9). The residual is small compared to the other monthly carbon fluxes (about 5% (7%) of the average value of the flux for each month for the ASZ (SIZ)), which gives us more confidence in our results. We also estimate an uncertainty for each monthly budget term.

To estimate the uncertainty associated with the results of the mixed layer budgets, we use a Monte Carlo simulation with 1500 iterations. The uncertainty and degree of correlation of each data variable used in the simulation can be found in Table A1. The uncertainty associated with each budget result is set to one standard deviation of the mean of the 1500 simulations. We use a uniform distribution for the error in T,S,P and a normal distribution for all other variables. To estimate the uncertainty on the monthly composite of wind stress from ERA5, we interpolate the x- and y-direction wind stress at each front location for each ensemble member available from ERA5. We set the uncertainty as one standard deviation from the mean of the ensemble members. Similarly for the sea ice fraction from ERA5, we set the uncertainty of the change in sea ice fraction over a month as one standard deviation from the mean of the ensemble members. We use the uncertainty estimates provided by the LIAR algorithm for the uncertainty in TA (Carter et al., 2018). We set the uncertainty of the geostrophic velocity interpolated at each (latitude, longitude) location of the fronts to be 20% of the velocity, which is a conservative estimate based on the methodology (Gray & Riser, 2014).

Among the 1500 iterations of the Monte Carlo simulation, 8% (25%) of the eddy diffusivities (or κ_z) identified by the optimization scheme is negative for the ASZ (SIZ). This indicates up-gradient eddy diffusion of carbon which is not expected. However, when taking all iterations together, the averaged value of κ_z does converge to a positive value of the expected magnitude, as is also the case when running the budget with no uncertainty added. The presence of negative values of eddy diffusivity points toward the fact that this system is physically fragile and may flip to a different, maybe non physically realistic, state easily. This fragility probably originates from the identification of the MLD, which is sensitive to the addition of uncertainties to the temperature and salinity profiles.

The budget framework assumes that the biological processes taking up or releasing DIC in the mixed layer are only photosynthesis and respiration. However, formation and dissolution of calcium carbonate by certain phytoplankton species also changes the mixed layer DIC and alkalinity content while not influencing the oxygen content (Krumhardt et al., 2020). This process is not accounted for in our budget, which is a reasonable assumption for the ASZ and SIZ where there is low abundance of calcifying organisms (Balch et al., 2016).

In this study, DIC concentration is calculated from in situ pH and empirically-estimated alkalinity. Most of the uncertainty in the DIC concentration arises from the uncertainty in TA provided by the LIAR algorithm, which is defined for each depth and latitude-longitude position. We then propagate this uncertainty through the Monte-Carlo simulation, assuming that the uncertainty is random to avoid introducing spurious variability in our results. We should note, however, that the TA uncertainty may be correlated in time, at least seasonally. Testing the algorithm against seasonally resolved measurements would be required to determine how much of the uncertainty is correlated in time. As such, the uncertainty on the DIC fluxes may be underestimated here.

4 Results

4.1 Drivers of the annual-mean mixed layer carbon budget

We first consider the drivers of the annually integrated air-sea flux of carbon in the high-latitude Southern Ocean (Fig. 2 b)). Note that the tendency term of Eq. 3 integrates to 0 by definition and does not appear in the annually integrated results. We find a net outgassing of carbon in both zones. In the ASZ, the outgassed carbon enters the mixed layer by eddy-driven mixing with carbon-rich waters from the interior. This DIC is then either consumed by net community production or outgassed to the atmosphere. The magnitudes of the annual advective and entrainment fluxes are small. In the SIZ, the annual fluxes of DIC are of smaller magnitude in general than those in the ASZ. Similarly to the more northerly region, the annually-averaged contribution from the entrainment flux is small, and DIC principally enters the mixed layer due to a mixing flux from below. However, since the outgassing signal is weak and the annual biological flux adds DIC to the mixed layer (due to net community respiration), the surplus of carbon is carried north to the ASZ by net Ekman transport.

If the supply of DIC from the SIZ was decreased, the Ekman transport leaving the ASZ at the northern front would overwhelm the vertical advection of DIC into the mixed layer (Fig. 2 a)). Thus, the Ekman flux of DIC from the SIZ supports an outgassing signal in the ASZ by making the total advective flux in the ASZ a small source of carbon and not a sink. Since the magnitude of the individual advective fluxes is so much greater than the net DIC advection (Fig. 2 a)), changes in the transport at the southern front may be critical in determining the net air-sea flux of carbon dioxide in this region.

4.2 Seasonally-varying fluxes of carbon in the mixed layer

The monthly-averaged fluxes reveal similar seasonal patterns in air-sea carbon flux across both high-latitude regions, with carbon uptake by the ocean in summer partly opposing carbon outgassing during the rest of the year (Fig. 3 and 4). In the ASZ, the air-sea flux is stronger and peaks at the end of winter (September), while in the SIZ carbon outgassing is strongly modulated by sea ice concentration and peaks in May (Butterworth & Miller, 2016).

We find that the seasonal variations in carbon air-sea flux lag one to two months behind the contribution from the term obtained by subtracting the entrainment from the tendency term (TEND-$F_{entrain}$, Fig.3 and 4). This relationship is confirmed by a strong anticorrelation of -0.93 (-0.83) or -0.88 (-0.87) at one or two months lag for the ASZ (SIZ). The TEND-$F_{entrain}$ term is equivalent to the time rate of change of the mixed layer concentration multiplied by the mixed layer depth (see Eq. 7). Both the TEND and $F_{entrain}$ are two orders of magnitude larger than the other fluxes (not shown). However, their net effect is much smaller and comparable to the other processes that change the mixed layer DIC. Since the seasonal cycle in mixed layer depth is only weakly correlated to the seasonal cycle in TEND-$F_{entrain}$ (0.39 and 0.45 for the ASZ and SIZ respectively, Fig.S2), we interpret seasonal variations in TEND-$F_{entrain}$ to be caused by variations

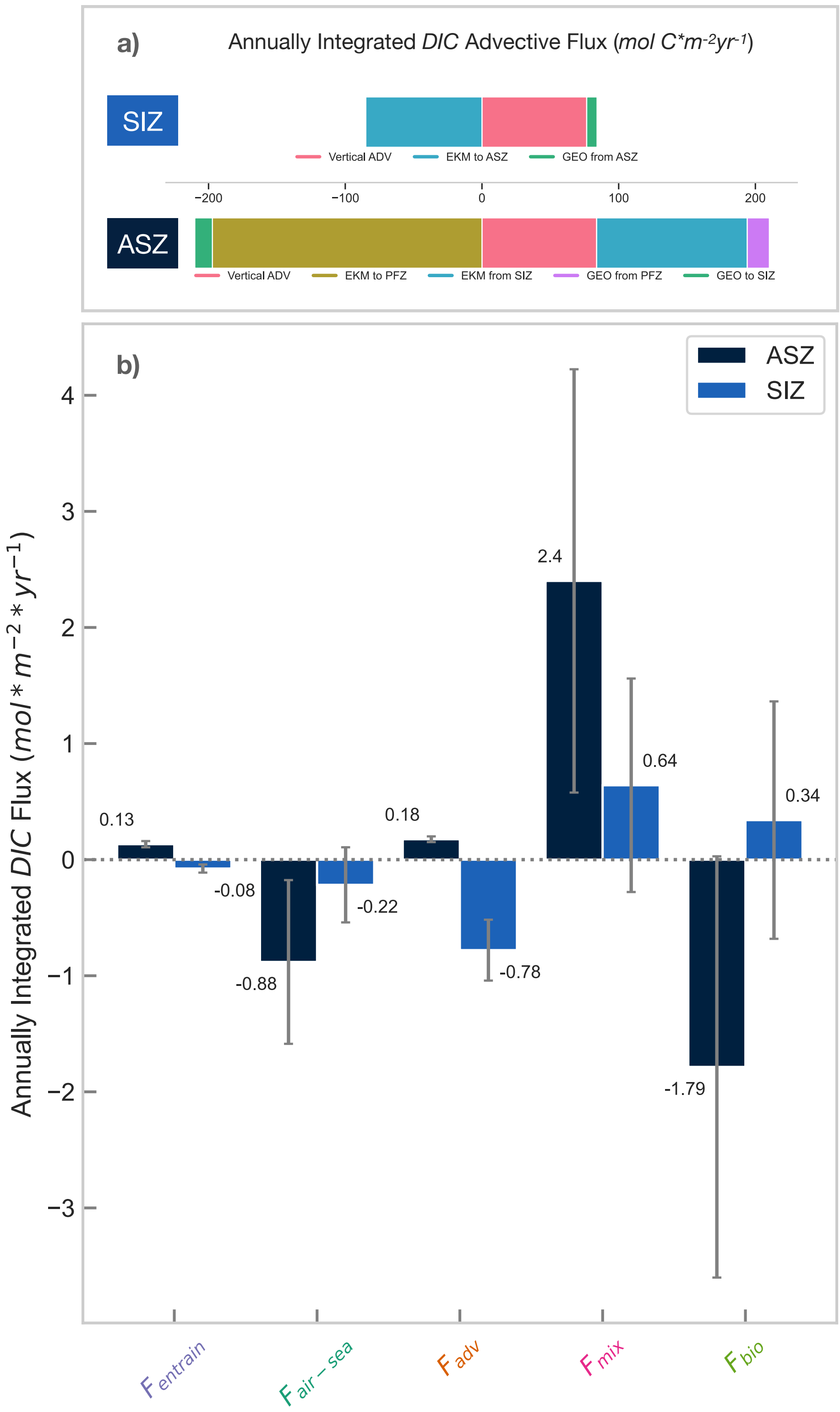

Figure 2. a) Annually integrated advective fluxes of DIC which add up to F_{adv} (uncertainty is not shown because error bars are too small). b) Annually integrated fluxes of DIC and their uncertainty indicated by the gray bars. Negative values indicate that DIC is being removed from the mixed layer of the zone in question ($F_{entrain}$: Entrainment flux, $F_{air-sea}$: Air-sea flux, F_{adv}: Advective flux, F_{mix}: Mixing flux, F_{bio}: Biological flux) (ASZ: Antarctic Southern Zone, SIZ: Sea Ice Zone)

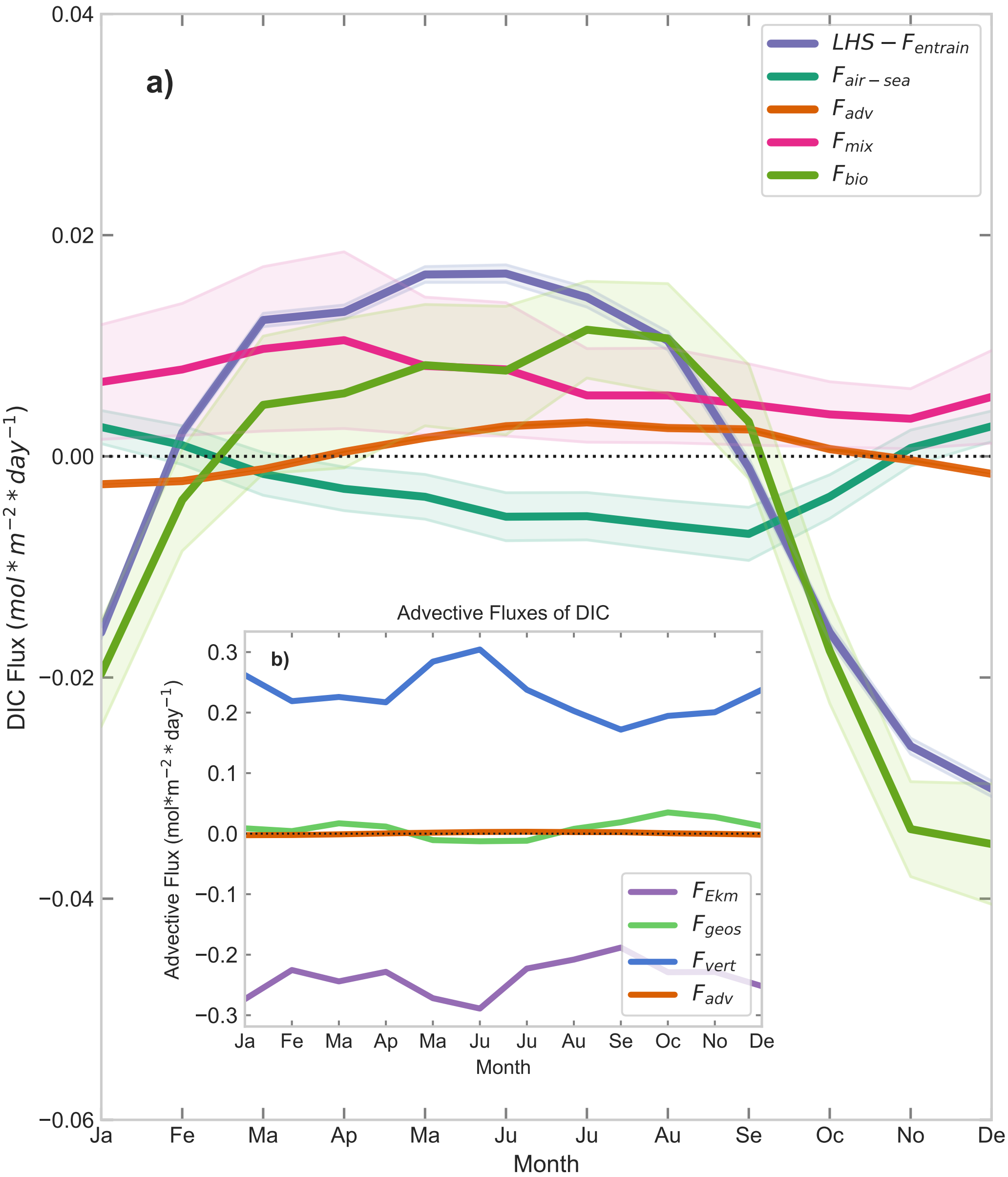

Figure 3. Monthly averaged fluxes of DIC to and from the ASZ mixed layer. a) DIC fluxes are presented with their uncertainty of one standard deviation. b) The components of the advective flux are presented: the flux of DIC due to Ekman advection (F_{Ekm}), geostrophic advection (F_{geos}), vertical advection (F_{vert}), as well as the net advective flux of DIC (F_{adv}). Uncertainty on the components of the advective flux is very small. Negative (positive) fluxes remove (add) carbon from (to) the mixed layer.

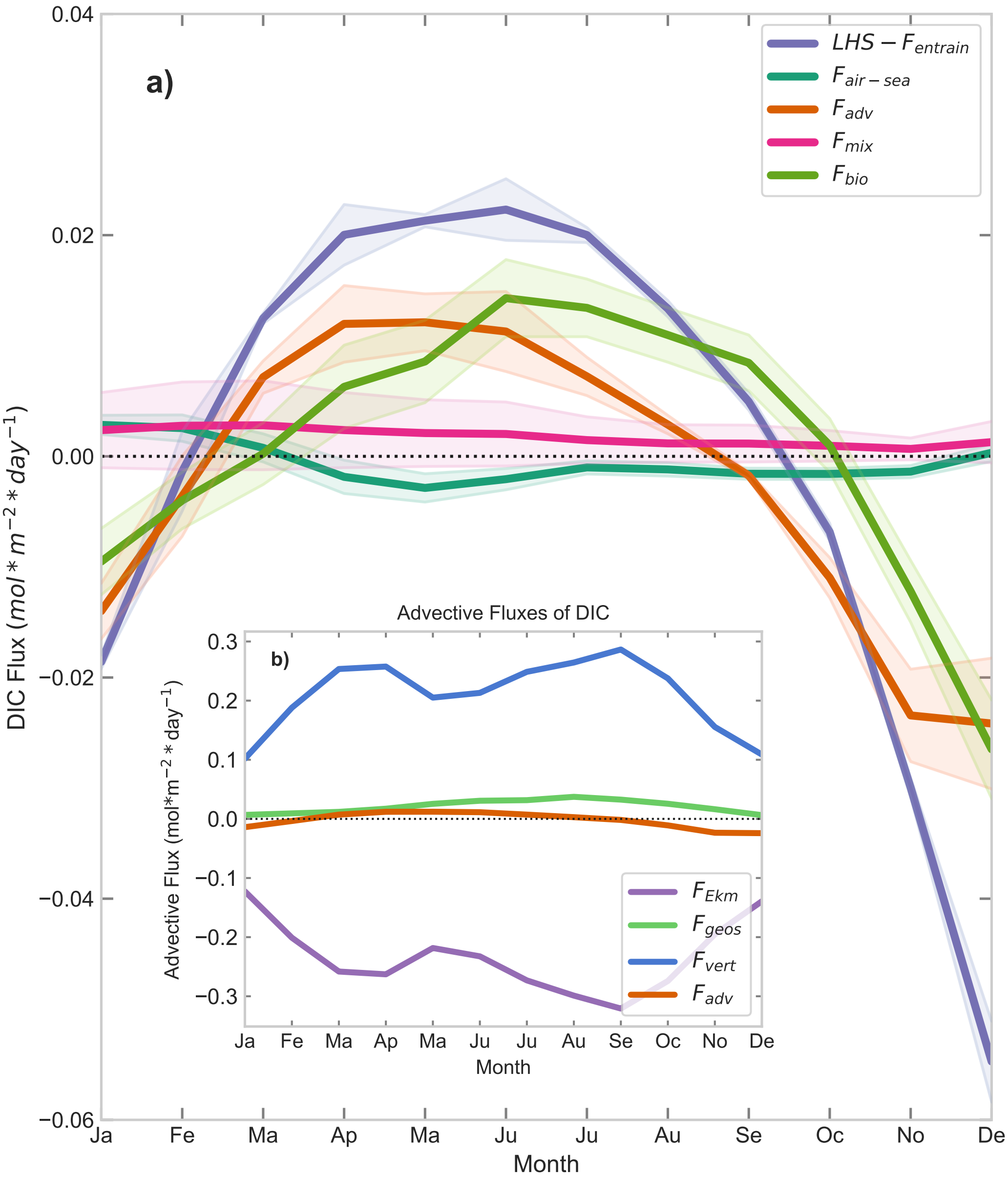

Figure 4. Monthly averaged fluxes of DIC to and from the SIZ mixed layer. a) DIC fluxes are presented with their uncertainty of one standard deviation. b) The components of the advective flux are presented: the flux of DIC due to Ekman advection (F_{Ekm}), geostrophic advection (F_{geos}), vertical advection (F_{vert}), as well as the net advective flux of DIC (F_{adv}). Uncertainty on the components of the advective flux is very small. Negative (positive) fluxes remove (add) carbon from (to) the mixed layer.

in the rate of change of mixed layer DIC concentration. Periods of carbon outgassing (uptake) tend to follow periods of concentration increase (decrease) by about one month, suggesting that changes in mixed layer DIC concentration are driving the air-sea fluxes of carbon in the frontal regions under study (Gruber et al., 2019). To support the link between carbon air-sea fluxes and surface DIC concentration, we examine the drivers of pCO_2 seasonal variability by computing pCO_2 in pyCO2SYS while varying only one variable at a time. We find that in the high-latitude Southern Ocean, nearly all variability is due to seasonal changes in pH and thus to changes in DIC (Fig. S17).

Seasonal variations in the mixed layer DIC concentration change are driven chiefly by changes in the biological flux term in both zones (Fig. 3 and 4), as confirmed by a strong correlation of 0.97 and 0.95 at no lag for the ASZ and SIZ, respectively. Biological activity adds carbon to the mixed layer when DIC concentration is increasing, probably due to net respiration, and the biological flux removes carbon from the mixed layer during the spring and summer phytoplankton bloom. The strength of this bloom is greater in the ASZ, as can be seen by the strong drop in the biological flux between September and November. In the SIZ, the seasonal cycle of the advective flux (Fig. 4) is just as important as variations in the biological flux in driving changes in mixed layer DIC concentration (correlation of 0.96 at no lag).

The net advective flux is the sum of the Ekman, vertical and geostrophic components (Fig. S6). We assume that the contribution from eddy-driven advection is small in the mixed layer for the timescales considered here. The individual advective components dominate over the other DIC fluxes (Fig. S13 and S14), but the Ekman and vertical components largely compensate so that the net advection is of smaller magnitude. We find a net positive advective flux of DIC in fall and winter, indicating a dominance of vertical advection over the net meridional advection, while the opposite occurs in summer and spring. In the ASZ, the magnitude of the advective flux is much smaller than the biological flux (Fig. 3), though we do observe a sign reversal similar to the SIZ, from net positive flux in winter to net negative flux in summer. In both zones, the flux of DIC from diffusive mixing with carbon-rich waters at the mixed layer base always acts to bring DIC into the mixed layer (Fig. 3 and 4). In the ASZ, the mixing flux acts to bring more DIC into the mixed layer than the biological flux during the fall period of DIC concentration increase. However, in both regions, the seasonal variations of the mixing flux are not strongly correlated with the change in DIC concentration.

In both zones, seasonal variations in the net advective flux of DIC can be attributed to a combination of changes in the Ekman flux of DIC from the SIZ to the ASZ and changes in the vertical advection signal, though the months where one or the other dominates are not the same across the study region (Fig. 5). Changes in the southward geostrophic transport of DIC are also correlated with changes in the net advection, but the magnitude of the geostrophic advection is one order of magnitude smaller than the Ekman and vertical advections (Fig. S13).

By comparing the period of carbon outgassing (April to August) to the period of carbon uptake (December to January), we gain further insight into what drives the seasonal fluxes in this region. During wintertime outgassing, the mixed layer DIC concentration is increasing (positive value of TEND-$F_{entrain}$, Fig. 3 and 4) because net respiration, eddy-driven mixing from below and net vertical advection bring DIC into the mixed layer. Some of this DIC is then outgassed to the atmosphere (Fig. 3 and 4). During the summer period of oceanic carbon uptake, the mixed layer DIC concentration is decreasing due to strong net photosynthesis and a net Ekman northward advection of DIC. This superposition of processes leads to carbon uptake from the atmosphere (Fig. 3 and 4). However, mixing with carbon-rich waters below is still bringing DIC into the mixed layer, which may contribute to the observed net outgassing signal over a full seasonal cycle.

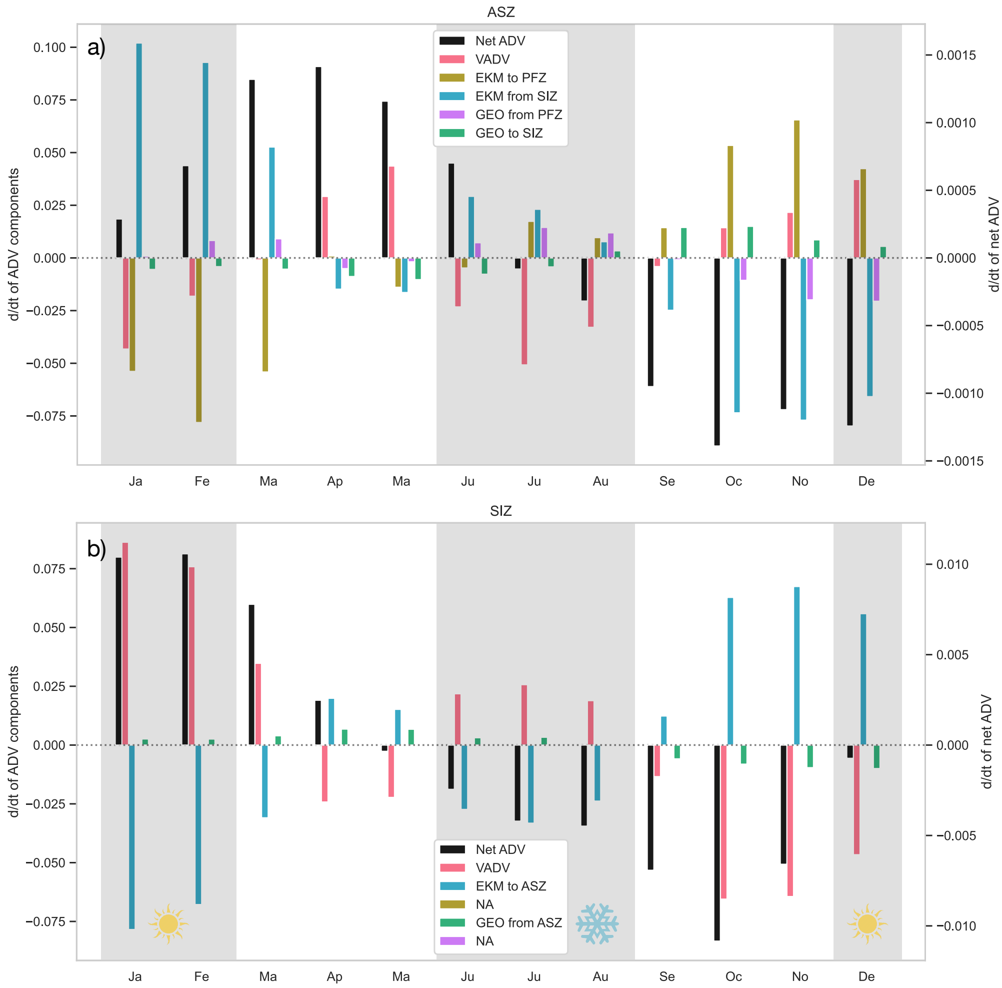

Figure 5. First time-derivative of the monthly averaged advective fluxes of DIC for a) the ASZ and b) the SIZ (mol m^{-2} day^{-1} month^{-1}). Note that the net advective flux (Net ADV) is plotted on its own axis (right) and the components of the net advective flux (Ekman (EKM), geostrophic (GEO) and vertical (VADV) advective fluxes of DIC) are plotted on the left axis. The gray shading indicates the summer and winter months.

The shift from carbon outgassing to uptake corresponds to a shift from respiration to photosynthesis and from net positive to net negative advection (Fig. 3 and 4). In the ASZ, the net advective flux of DIC primarily changes sign because of transport at the southern front; namely, Ekman advection of DIC from the SIZ (Fig. S13 and S14) decreases significantly from winter to summer (by 53% on average), while the vertical advective flux and Ekman transport at the northern front stay relatively constant (decreases by 15% and 28% respectively). In the SIZ, most components of the advective flux decrease by approximately half during months of carbon uptake compared to months of outgassing.

The seasonal change in the Ekman advective flux of DIC at the sea ice front is due to changes in Ekman mass transport driven by wind variations, rather than changes in the DIC concentration of the SIZ. We observe that the seasonal cycle in the Ekman mass advection and its components is very similar to that of the Ekman DIC advection (Fig. S15 and S16). Furthermore, the amplitude of seasonal variations of the Ekman mass advection at the SIF is 74% (83%) for the ASZ (SIZ) which compares well to the amplitude of seasonal change of the Ekman DIC advection at the SIF (76% (85%) for the ASZ (SIZ)), while the amplitude of seasonal variations in the mixed layer DIC concentration of the SIZ used to convert mass transport to DIC advection is only 3% in both zones.

5 Discussion

Using a monthly mixed layer carbon budget of the high-latitude Southern Ocean, we show that small-scale mixing at the base of the mixed layer provides DIC to the surface layer year-round. In the ASZ, most of this DIC is then consumed by net biological production, while the net biological flux is not significantly different from zero in the SIZ. On an annual timescale, the surplus of DIC in the mixed layer from the balance of these two processes is either advected from the SIZ to the ASZ by Ekman divergence or outgassed to the atmosphere in the ASZ. Physical transport of carbon, in concert with the transition from net production to net respiration, also explains the difference between seasonal periods of carbon outgassing (fall to spring) and uptake (summer).

Values for the vertical eddy diffusivity at the base of the mixed layer are sparse in the literature. Still, the magnitude of the diffusivity obtained from our optimization scheme (between 1.48 and 8.68×10^{-5} m^2/s) is similar to the only comparable published value in the Southern Ocean (less than 3×10^{-5} m^2/s) (Law et al., 2003). The ASZ makes up the southern part of the ACC, where wind-driven upwelling brings carbon-rich isopycnals to the near-surface. The high-latitude Southern Ocean also exhibits strong vertical DIC gradients (Dove et al., 2022); therefore, it is not surprising that subsurface mixing plays a strong role in supplying DIC to the mixed layer. In the SIZ, there is also upwelling of carbon-rich deep waters. However, the SIZ is characterized by multiple gyre circulations as well as sea ice cover, which can act to isolate the surface ocean from the atmosphere and may be a barrier to momentum transfer (Shadwick et al., 2021; Vihma & Haapala, 2009). Indeed, we find a stronger mixing flux of DIC in the ASZ compared to the SIZ due to differences in the eddy diffusivity (see Section A3), consistent with more wind energy input in the ASZ resulting from stronger winds and lack of ice cover. However, the vertical gradient of DIC near the base of the mixed layer is stronger in the SIZ, most probably due to gyre dynamics allowing respired DIC to accumulate in the surface waters (MacGilchrist et al., 2019).

We find that inorganic carbon entering the mixed layer through eddy processes is mostly consumed by biological production. This is similar to previous results by Hauck et al. (2013), who found that biological processes remove more DIC from the mixed layer than air-sea fluxes. In the ASZ specifically, annual net production is the dominant sink of DIC in the mixed layer. We find annual net production of 1.79 mol C m^{-2} yr^{-1} in this region, consistent with previous float-based annual net community production estimates at similar latitudes (about 1-2 mol C m^{-2} yr^{-1}) (Arteaga et al., 2019). In the SIZ, however, we find annual net respiration, which is different from model-based results (Carroll et al., 2022). Note though that error bars are large and extend to a small value of net production. This result, similar to the analysis of Briggs et al. (2018) who found that respiration in winter nearly balanced out biological production, could reflect a flux of organic carbon from production by sea ice algae (Arrigo et al., 1997; Saenz & Arrigo, 2014). In addition, a missing flux of DIC from the Antarctic continental shelf or from icebergs may be contributing to the net respiration determined by the optimization process if the missing signal has a similar seasonal pattern. Still, in both zones, we find an important net production signal in spring and summer and that the DIC tendency tends to follow the biological flux, as has been reported in past studies (Carroll et al., 2022; Yang et al., 2021; Williams et al., 2018). In winter in both zones, we find net respiration of the same order of magnitude as the seasonal photosynthesis signal, due to low light availability (even more significant for the SIZ).

In the SIZ, the role of DIC advection is as important as the biological flux in both the seasonal and annual budgets. In the annual view, the surplus of DIC from subsurface mixing is mostly advected to the ASZ by the Ekman transport component, rather than being consumed by the net biological flux or outgassed. This is likely due, in part, to the wintertime ice cover preventing (or limiting) outgassing, as the surface ocean $p\mathrm{CO}_2$ values alone imply a stronger outgassing than is observed. Indeed, a sea ice capping effect has been reported on the continental shelf (Shadwick et al., 2021) and in idealized models (Gupta et al., 2020). Still, without physical transport removing available DIC from the region in winter, there would be less potential for carbon uptake in summer after the sea ice melts. As such, seasonal variability in the net advective flux is important for explaining the low annual outgassing signal in the SIZ. Throughout the year, vertical advection supplies carbon to the mixed layer, while horizontal advection (dominated by Ekman divergence) removes DIC from the region. Net advection is the smaller residual of these two opposing processes. In summer and fall, the DIC flux due to vertical advection dominates over the Ekman transport (Fig. S14). In winter, however, stronger winds drive an increase in the Ekman flux of DIC, which continues until the net advection of DIC changes sign around the beginning of spring.

In the ASZ, seasonal variability in the advective flux of DIC from the SIZ is essential to explain the carbon air-sea fluxes in the region. In the annually-integrated view, the net advective flux in the ASZ is the residual between DIC removal from lateral advection at the northern front and DIC supply by both vertical advection and horizontal advection from the SIZ (Fig. 3). The different components of the advective flux depend on both the circulation and the DIC concentration of the source waters. These two aspects are connected but could evolve independently under future warming. For example, ice retreat could increase wintertime outgassing in the SIZ, subsequently reducing the northward Ekman flux of DIC and carbon outgassing in the ASZ. In the seasonal picture, the net advective flux of DIC is smaller in magnitude than some of the other fluxes (Fig. 3). Still, the change in sign of the net advection from periods of outgassing to uptake, which is due to a decrease in the amount of DIC entering from the SIZ by Ekman transport (Fig. S13), implies that wind-driven advection of DIC from the seasonal ice zone plays an important role in driving carbon outgassing in the ACC.

It is challenging to compare these results with previous work as there has been no other observation-based circumpolar mixed layer DIC budget in the Southern Ocean. However, a regional study of the Weddell Gyre (part of the SIZ) based on shipboard data and an inverse model found that DIC entrained from below mostly exits the gyre through northward transport to the ACC frontal region (equivalent to the ASZ) or becomes deep water at the gyre edges (Brown et al., 2015). Comparison to model-based DIC budgets is also difficult since they are typically computed over fixed depths, and many models have seasonal variations in air-sea carbon fluxes that are inconsistent with observations

(Mongwe et al., 2018). Still, two recent papers found that the advective flux of DIC plays an important role in the carbon budget of the region (Rosso et al., 2017; Carroll et al., 2022). For example, Carroll et al. (2022) find that the DIC tendency and interannual variability in their SIZ biome is dominated by net advection, although they do not show the contribution from the different advective components. Rosso et al. (2017) do separate the advection into vertical, geostrophic and ageostrophic components, however, they compute their budget down to 650m, which implicitly reduces the relative importance of Ekman transport (which only occurs in the top ∼80m). One study did find, using a high-resolution model, that Ekman transport was the primary mechanism for the zonally integrated, cross-frontal transport of anthropogenic CO_2 and its intra-annual variability, particularly across the polar front (Ito et al., 2010).

While these studies support our own results, they do not directly confirm the importance of Ekman transport from the SIZ in driving carbon outgassing in the southern ACC. In fact, while estimates based on biogeochemical float data find net outgassing in the high-latitude Southern Ocean that peaks in winter (Gray et al., 2018), this result disagrees with estimates based on shipboard $p\mathrm{CO}_2$ measurements (Takahashi et al., 2009; Landschützer et al., 2014; Gruber et al., 2019), airborne measurements (Long et al., 2021) and ocean biogeochemical circulation models (Hauck et al., 2022). We use the carbon air-sea flux estimates from the SeaFlux ensemble data product, which is primarily based on ship-board observations (Fay et al., 2021; Gregor & Fay, 2021), as input in our analysis in order to further investigate how carbon uptake in this region would impact the resulting mixed layer budgets. We find that the mixing and biological fluxes identified by the optimization scheme are not in line with previous work when using the SeaFlux-based air-sea fluxes (Fig. S10, S11 and S12). In the SIZ, the mixing flux is negative due to a negative vertical eddy diffusivity, indicating diffusive mixing towards regions of higher concentration. In the ASZ, the annually-integrated biological flux at 3.55 mol C m^{-2} yr^{-1} is much higher than expected based on previous estimates (Fig. S10) (Arteaga et al., 2019). These results imply that carbon uptake of the magnitude found in the SeaFlux-based air-sea fluxes is not only inconsistent with the float-based DIC budgets but also with the float-based oxygen observations that are used in the optimization scheme. This discrepancy is likely due, at least in part, to the availability of year-round float data, whereas shipboard observations are seasonally-biased except in Drake Passage.

6 Conclusion

We use six years of under-ice capable autonomous biogeochemical float data to construct a monthly mixed layer carbon budget in two regions of the high-latitude Southern Ocean. We find that the monthly changes in the mixed layer DIC concentration closely corresponds to the seasonal variations in the biological flux of DIC. However, northward Ekman transport from the SIZ is also significant in setting the seasonal changes in DIC concentration. On annual timescales, mixing with carbon-rich waters from below the mixed layer leads to carbon outgassing in both regions under study (Fig. 6). However, in the SIZ, where ice cover damps air-sea exchange and primary production is heavily light-limited, most of the carbon injected from below the mixed layer is transported northward to the ASZ by Ekman advection. In other words, Ekman transport of DIC from the seasonal ice zone contributes to carbon outgassing in the southern portion of the ACC. This has implications for the response of the Southern Ocean carbon cycle to anthropogenic forcing, since reduced ice cover under ocean warming could potentially lead to a redistribution of carbon outgassing from the ASZ to the SIZ.

These results comprise the first observation-based carbon budget spanning large spatial scales and at monthly resolution in the high-latitude Southern Ocean. Strong seasonal variability in air-sea fluxes, as well as biological and advective fluxes of carbon, highlight the importance of year-round measurements in understanding carbon cycling in the region. These results also provide a much-needed observational baseline to evaluate the

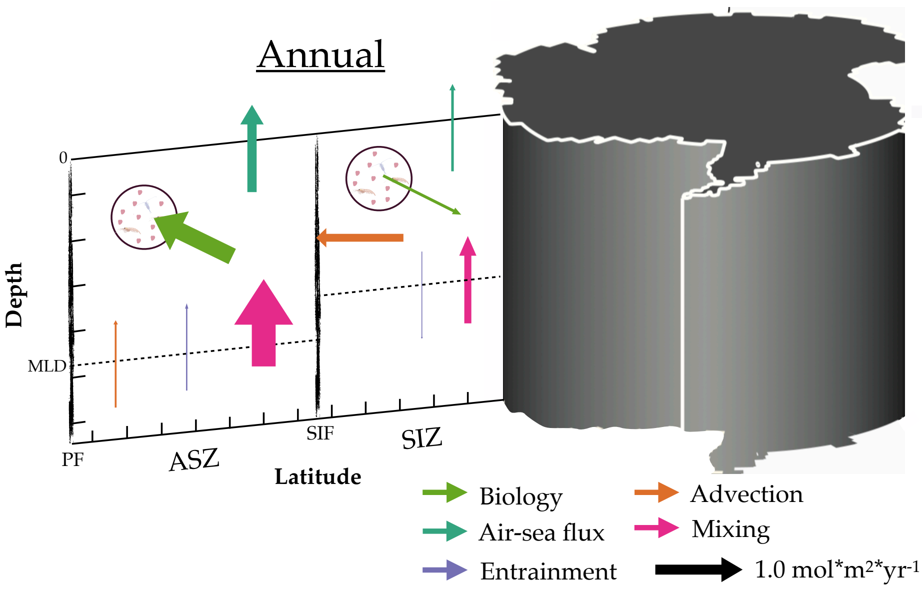

Figure 6. Schematic of the annually integrated fluxes of carbon where each colored arrow correspond to a different process by which the DIC content of the mixed layer can be modified. The green arrow represents the net effect of biological activity on mixed layer DIC content. The teal arrow represents the air-sea flux of carbon. The purple arrow corresponds to the entrainment flux of DIC. The orange arrow represents the net advective flux of DIC by Ekman, geostrophic and vertical advection. The pink arrow represents the eddy-driven mixing flux of DIC. The width of each arrow scales with the magnitude of the flux. (ASZ: Antarctic Southern Zone, SIZ: Sea Ice Zone)

performance of climate models, which are notably unsuccessful in reproducing the Southern Ocean carbon cycle (Hauck et al., 2020). Improved understanding of these processes is crucial given the key role of the Southern Ocean in the global climate system.

Appendix A Additional Method Information

A1 Horizontal Mass Transport

The monthly averaged Ekman mass transport is northward at the SIF and PF which is as expected due to the presence of strong westerly winds at those latitudes (Fig. S4). The monthly Ekman transport averages to 20.2 Sv at the SIF and 36.5 Sv at the PF, which is consistent with previous modeling studies that found a zonally integrated Ekman transport along 60°S (50°S) of 25 Sv (55 Sv) (Hallberg & Gnanadesikan, 2006). There is about twice as much transport (varying from 1.5x to 2.8x) across the PF than the SIF, which is not surprising as wind driven transport can be inhibited by the presence of sea ice.

Monthly averaged mixed layer geostrophic transport is southward for the SIF and the PF, and it is one order of magnitude smaller than the monthly averaged Ekman transport, with an average of -2.4 Sv (panel b) of Fig. S4). We present mixed layer geographic transport separately for each zonal regions on either side of one front due to our choice of depth of integration. In the Ekman transport calculation, we assume that the Ekman depth is shallower than the mixed layer depth, an assumption which is likely true for most months but may break down in summer or fall depending on the eddy viscosity (not shown). This assumption allows us to consider the full depth of the Ekman layer and removes the need to choose a depth of integration. For the geostrophic transport calculation, we integrate the geostrophic velocity down to the mixed layer depth of the region under consideration.

We do not consider the eddy component of the horizontal advection in this region as it has been shown to be more than 50% smaller than the time mean component in the Ekman layer (Dufour et al., 2015).

A2 Mass Budget and Vertical Velocity

The seasonal cycle of the monthly averaged mixed layer mass fluxes differs between the ASZ and the SIZ (Fig. S6). However, we observe that there is a balance between the surface fluxes of mass and the advective mass flux in both frontal regions while the term representing the difference between the tendency and the entrainment ($TEND - F_{entrain}$) is negligible. In the ASZ, the fluxes of mass do not vary strongly from month to month. Surface fluxes of mass, including precipitation, evaporation and a small contribution from sea ice melt and freeze, lead to water accumulating in the region's mixed layer. This is balanced by a mass advection out of the ASZ. The sign of the advective flux is set by a balance between the negative Ekman advection and the positive vertical advection (Fig. S6). The geostrophic advection is at least one order of magnitude smaller. In the SIZ, the sea ice melt and freeze cycle creates strong seasonal variations in the monthly averaged surface flux which leads to seasonal variations of similar magnitude but opposite sign in the advective flux. As such, we see a positive advective flux of mass (driven by vertical advection) during ice formation and a negative advective mass flux (driven by Ekman advection) during sea ice melt. On annual time scales, mass fluxes in the SIZ and the ASZ are similar with a positive surface flux opposed by a negative advective flux driven by a dominance of Ekman transport out of the zone over vertical mass advection into the mixed layer (Fig. S7).

Using the mixed layer mass budget, we solve for the vertical velocity at the base of the mixed layer (w_{-h}) which is shown in Fig. S3. We find an average w_{-h} of 1.19×

$10^{-6} m/s$ ($1.07 \times 10^{-6} m/s$) in the ASZ (SIZ). This vertical velocity is of the expected scale and sign for these two frontal regions where upwelling is expected (Gruber et al., 2019). Because we have used a mass budget to estimate w_{-h}, our estimate includes both the effect of Ekman upwelling and other processes such as topography-driven or storm-driven upwelling.

A3 Estimated Parameters

We solve a non-linear system composed of the different monthly averaged budget equations for DIC and O_2 to find the missing parameters: the eddy diffusivity (κ_z), the respiration quotient (R_{O_2}) and the monthly biological flux of DIC (F_{bio}). We find an eddy diffusivity of $(8.68 \pm 6.9) \times 10^{-5}$ m^2 s^{-1} ($(1.48 \pm 2.2) \times 10^{-5}$ m^2 s^{-1}) for the ASZ (SIZ) (see Sections 3.5 and 5 for more information). We find a respiratory quotient of -0.63 ± 0.17 (-1.72 ± 0.21) for the ASZ (SIZ). The canonical value for the oxygen to carbon ratio is -1.45 (Anderson & Sarmiento, 1994). However, DeVries and Deutsch (2014) found important latitudinal variations in the amount of oxygen consumed by unit of phosphate released during respiration ($R_{O_2/P}$). In the high-latitude Southern Ocean in particular, they find that $R_{O_2/P}$ increases from about 50 to 200 between 47°S and 70°S. When we convert $R_{O_2/P}$ to the respiratory quotient ($R_{O_2/C}$) using 106C:P, we find that we see a latitudinal variation of similar magnitude from the ASZ to the SIZ. The magnitude of the monthly averaged biological flux of DIC obtained from the optimization scheme and its clear seasonal cycle are as expected with a strong uptake of carbon during the spring bloom, stronger in the ASZ than in the SIZ (Fig. S5). The positive flux of carbon in winter, indicating dominance of respiration over photosynthesis, can be explained by the severe light and micro-nutrient limitations in the high-latitude Southern Ocean.

A4 Error and Correlation of each Variable used in Monte Carlo Simulation

We record the error and correlation of each variable used in the Monte Carlo simulation in Table 1.

Open Research

The quality-controlled data from the 22 December 2020 SOCCOM snapshot are used in this analysis (`http://doi.org/10.6075/J0B27ST5`). We also utilize the European Centre for Medium-Range Weather Forecasts (ECMWF) ERA5 atmospheric reanalysis product (`https://cds.climate.copernicus.eu/`), the SeaFlux harmonized sea-air CO_2 fluxes (`10.5281/zenodo.4133802`), the Roemmich-Gilson Argo Climatology (`https://sio-argo.ucsd.edu/RG_Climatology.html`), and the ETOPO1 Global Relief Model (`http://dx.doi.org/10.7289/V5C8276M`).

Acknowledgments

This work was supported through National Science Foundation grants OPP-193622 (SOCCOM) and awards 1946578 (GO-BGC) and 2110258 (GO-BGC Operational Support). Additionally, we acknowledge the generous continuing support of NOAA through grant NA20OAR4320271 (US Argo). JS was also partly supported by a University of Washington Program on Climate Change fellowship. CJP also received funding through a NOAA Climate & Global Change Postdoctoral Fellowship. ARG acknowledges additional support from NSF through award OCE-1756882 and from the Department of Energy through Award DE-SC0022243. Profiling float data were collected and made freely available by the Southern Ocean Carbon and Climate Observations and Modeling (SOCCOM) Project funded by the National Science Foundation, Division of Polar Programs (NSF PLR-1425989), supplemented by NASA (NNX14AP49B), and by Argo and the NOAA programs that

Table A1. Error and Correlation of each Variable used in Monte Carlo Simulation

Variable	Error	Unit	Correlation	Source
T	0.002	°C	uncorrelated	(Wong et al., 2020)
S	0.01	PSU	uncorrelated	(Wong et al., 2020)
P	2.4	dbar	uncorrelated	(Wong et al., 2020)
O_2	3	μmol/kg	uncorrelated	(Johnson et al., 2017)
TA	8.74*	μmol/kg	uncorrelated	(Carter et al., 2018)
pH	0.007	total	uncorrelated	(Johnson et al., 2017)
N	0.5	μmol/kg	uncorrelated	(Johnson et al., 2017)
ΔSIC_{SIZ}	3.45×10^8*	m^2/day	uncorrelated	(Hersbach et al., 2020)
ΔSIC_{ASZ}	4.23×10^7*	m^2/day	uncorrelated	(Hersbach et al., 2020)
SIT	20%	N/A	uncorrelated	(Li et al., 2018)
(Precip. - Evap.)	1.24×10^{-7}*	kg/m^2/s	uncorrelated	(Hersbach et al., 2020)
$(\tau_x/\rho f)_{inter}$	0.00246*	m^2/s	uncorrelated	(Hersbach et al., 2020)
$(\tau_y/\rho f)_{inter}$	0.00167*	m^2/s	uncorrelated	(Hersbach et al., 2020)
$\vec{u}_{geo-inter}$	20%	N/A	uncorrelated	(Gray & Riser, 2014)
$F_{air-sea-C}$	0.506*	mol/m^2/yr	correlated in time	(Gray et al., 2018)
$F_{air-sea-O_2}$	20%	N/A	correlated in time	(Bushinsky et al., 2017)

[a] *average error from field of individual errors

contribute to it. The Argo data were collected and made freely available by the International Argo Program and the national programs that contribute to it. (http://www.argo.ucsd.edu, http://argo.jcommops.org). The Argo Program is part of the Global Ocean Observing System. Input from B. Carter and N. Williams is gratefully acknowledged.

References

Amante, C., & Eakins, B. (2009). *ETOPO1 1 Arc-Minute Global Relief Model: Procedures, Data Sources and Analysis* (Tech. Rep.). National Geophysical Data Center, NOAA. doi: 10.7289/V5C8276M

Anderson, L. A., & Sarmiento, J. L. (1994). Redfield ratios of remineralization determined by nutrient data analysis. *Global Biogeochemical Cycles*, *8*(1), 65–80. Retrieved from `https://agupubs.onlinelibrary.wiley.com/doi/abs/10.1029/93GB03318` doi: 10.1029/93GB03318

Arrigo, K. R., Worthen, D. L., Lizotte, M. P., Dixon, P., & Dieckmann, G. (1997). Primary Production in Antarctic Sea Ice. *Science (American Association for the Advancement of Science)*, *276*(5311), 394–397.

Arteaga, L. A., Pahlow, M., Bushinsky, S. M., & Sarmiento, J. L. (2019). Nutrient Controls on Export Production in the Southern Ocean. *Global Biogeochemical Cycles*, *33*(8), 942–956. Retrieved from `https://agupubs.onlinelibrary.wiley.com/doi/abs/10.1029/2019GB006236` doi: 10.1029/2019GB006236

Balch, W. M., Bates, N. R., Lam, P. J., Twining, B. S., Rosengard, S. Z., Bowler, B. C., . . . Rauschenberg, S. (2016). Factors regulating the Great Calcite Belt in the Southern Ocean and its biogeochemical significance. *Global Biogeochemical Cycles*, *30*(8), 1124–1144. Retrieved from `https://agupubs.onlinelibrary.wiley.com/doi/abs/10.1002/2016GB005414` doi: https://doi.org/10.1002/2016GB005414

Branch, M. A., Coleman, T. F., & Li, Y. (1999). A Subspace, Interior, and Conjugate Gradient Method for Large-Scale Bound-Constrained Minimization Problems. *SIAM Journal on Scientific Computing*, *21*(1), 1–23. Retrieved from `https://doi.org/10.1137/S1064827595289108` doi: 10.1137/S1064827595289108

Briggs, E. M., Martz, T. R., Talley, L. D., Mazloff, M. R., & Johnson, K. S. (2018). Physical and Biological Drivers of Biogeochemical Tracers Within the Seasonal Sea Ice Zone of the Southern Ocean From Profiling Floats. *Journal of Geophysical Research: Oceans*, *123*(2), 746–758. Retrieved from `https://agupubs.onlinelibrary.wiley.com/doi/abs/10.1002/2017JC012846` doi: 10.1002/2017JC012846

Bronselaer, B., Zanna, L., Munday, D. R., & Lowe, J. (2018). Southern Ocean carbon-wind stress feedback. *Climate Dynamics*, *51*(7), 2743–2757. Retrieved from `https://doi.org/10.1007/s00382-017-4041-y` doi: 10.1007/s00382-017-4041-y

Brown, P. J., Jullion, L., Landschützer, P., Bakker, D. C. E., Naveira Garabato, A. C., Meredith, M. P., . . . Wanninkhof, R. (2015). Carbon dynamics of the Weddell Gyre, Southern Ocean. *Global Biogeochemical Cycles*, *29*(3), 288–306. Retrieved from `https://agupubs.onlinelibrary.wiley.com/doi/abs/10.1002/2014GB005006` doi: https://doi.org/10.1002/2014GB005006

Bushinsky, S. M., Gray, A. R., Johnson, K. S., & Sarmiento, J. L. (2017). Oxygen in the Southern Ocean From Argo Floats: Determination of Processes Driving Air-Sea Fluxes. *Journal of Geophysical Research: Oceans*, *122*(11), 8661–8682. Retrieved from `https://agupubs.onlinelibrary.wiley.com/doi/abs/10.1002/2017JC012923` doi: 10.1002/2017JC012923

Bushinsky, S. M., Landschützer, P., Rödenbeck, C., Gray, A. R., Baker, D., Mazloff, M. R., . . . Sarmiento, J. L. (2019). Reassessing Southern Ocean Air-Sea CO2 Flux Estimates With the Addition of Biogeochemical Float Observations.

Global Biogeochemical Cycles, *33*(11), 1370–1388. Retrieved from https://agupubs.onlinelibrary.wiley.com/doi/abs/10.1029/2019GB006176 doi: 10.1029/2019GB006176

Butterworth, B. J., & Miller, S. D. (2016). Air-sea exchange of carbon dioxide in the Southern Ocean and Antarctic marginal ice zone. *Geophysical Research Letters*, *43*(13), 7223–7230. Retrieved from https://agupubs.onlinelibrary.wiley.com/doi/abs/10.1002/2016GL069581 doi: https://doi.org/10.1002/2016GL069581

Carroll, D., Menemenlis, D., Dutkiewicz, S., Lauderdale, J. M., Adkins, J. F., Bowman, K. W., ... Zhang, H. (2022). Attribution of Space-Time Variability in Global-Ocean Dissolved Inorganic Carbon. *Global Biogeochemical Cycles*, *36*(3), e2021GB007162. Retrieved from https://agupubs.onlinelibrary.wiley.com/doi/abs/10.1029/2021GB007162 doi: https://doi.org/10.1029/2021GB007162

Carter, B. R., Feely, R. A., Williams, N. L., Dickson, A. G., Fong, M. B., & Takeshita, Y. (2018). Updated methods for global locally interpolated estimation of alkalinity, pH, and nitrate. *Limnology and Oceanography: Methods*, *16*(2), 119–131. Retrieved from https://aslopubs.onlinelibrary.wiley.com/doi/abs/10.1002/lom3.10232 doi: 10.1002/lom3.10232

Cronin, M. F., Pelland, N. A., Emerson, S. R., & Crawford, W. R. (2015). Estimating diffusivity from the mixed layer heat and salt balances in the North Pacific. *Journal of Geophysical Research: Oceans*, *120*(11), 7346–7362. Retrieved from https://agupubs.onlinelibrary.wiley.com/doi/abs/10.1002/2015JC011010 doi: 10.1002/2015JC011010

de Boyer Montégut, C., Madec, G., Fischer, A. S., Lazar, A., & Iudicone, D. (2004). Mixed layer depth over the global ocean: An examination of profile data and a profile-based climatology. *Journal of Geophysical Research: Oceans*, *109*(C12). Retrieved from https://agupubs.onlinelibrary.wiley.com/doi/abs/10.1029/2004JC002378 doi: 10.1029/2004JC002378

DeVries, T. (2014, jul). The oceanic anthropogenic CO2 sink: Storage, air-sea fluxes, and transports over the industrial era [Article]. *GLOBAL BIOGEOCHEMICAL CYCLES*, *28*(7), 631–647. doi: 10.1002/2013GB004739

DeVries, T., & Deutsch, C. (2014). Large-scale variations in the stoichiometry of marine organic matter respiration. *Nature Geoscience*, *7*(12), 890–894. Retrieved from https://doi.org/10.1038/ngeo2300 doi: 10.1038/ngeo2300

Dickson, A. G. (1990). Standard potential of the reaction: AgCl(s) + 12H2(g) = Ag(s) + HCl(aq), and and the standard acidity constant of the ion HSO4 in synthetic sea water from 273.15 to 318.15 K. *The Journal of Chemical Thermodynamics*, *22*(2), 113–127. Retrieved from https://www.sciencedirect.com/science/article/pii/002196149090074Z doi: https://doi.org/10.1016/0021-9614(90)90074-Z

Dove, L. A., Balwada, D., Thompson, A. F., & Gray, A. R. (2022, jul). Enhanced Ventilation in Energetic Regions of the Antarctic Circumpolar Current. *Geophysical Research Letters*, *49*(13), e2021GL097574. Retrieved from https://agupubs.onlinelibrary.wiley.com/doi/abs/10.1029/2021GL097574https://onlinelibrary.wiley.com/doi/10.1029/2021GL097574 doi: 10.1029/2021GL097574

Dufour, C. O., Griffies, S. M., de Souza, G. F., Frenger, I., Morrison, A. K., Palter, J. B., ... Slater, R. D. (2015). Role of Mesoscale Eddies in Cross-Frontal Transport of Heat and Biogeochemical Tracers in the Southern Ocean. *Journal of Physical Oceanography*, *45*(12), 3057–3081. Retrieved from https://doi.org/10.1175/JPO-D-14-0240.1 doi: 10.1175/JPO-D-14-0240.1

Dufour, C. O., Sommer, J. L., Gehlen, M., Orr, J. C., Molines, J.-M., Simeon, J., & Barnier, B. (2013). Eddy compensation and controls of the enhanced sea-to-air CO2 flux during positive phases of the Southern Annular Mode. *Global Biogeochemical Cycles*, *27*(3), 950–961. Retrieved from https://agupubs.onlinelibrary.wiley.com/doi/abs/10.1002/gbc.20090 doi: 10.1002/gbc.20090

Fay, A. R., Gregor, L., Landschützer, P., McKinley, G. A., Gruber, N., Gehlen, M., ... Zeng, J. (2021). Harmonization of global surface ocean pCO2 mapped products and their flux calculations; an improved estimate of the ocean carbon sink. *Earth System Science Data Discussions*, 1–32.

Gray, A. R., Johnson, K. S., Bushinsky, S. M., Riser, S. C., Russell, J. L., Talley, L. D., ... Sarmiento, J. L. (2018). Autonomous Biogeochemical Floats Detect Significant Carbon Dioxide Outgassing in the High-Latitude Southern Ocean. *Geophysical Research Letters*, *45*(17), 9049–9057. doi: 10.1029/2018GL078013

Gray, A. R., & Riser, S. C. (2014). A Global Analysis of Sverdrup Balance Using Absolute Geostrophic Velocities from Argo. *Journal of Physical Oceanography*, *44*(4), 1213–1229. Retrieved from https://journals.ametsoc.org/view/journals/phoc/44/4/jpo-d-12-0206.1.xml doi: 10.1175/JPO-D-12-0206.1

Gregor, L., & Fay, A. (2021, jul). *SeaFlux: harmonised sea-air CO2 fluxes from surface pCO2 data products using a standardised approach.* Zenodo. Retrieved from https://doi.org/10.5281/zenodo.5482547 doi: 10.5281/zenodo.5482547

Gruber, N., Landschützer, P., & Lovenduski, N. S. (2019). The Variable Southern Ocean Carbon Sink. *Annual Review of Marine Science*, *11*(1), 159–186. Retrieved from https://doi.org/10.1146/annurev-marine-121916-063407 doi: 10.1146/annurev-marine-121916-063407

Gupta, M., Follows, M. J., & Lauderdale, J. M. (2020). The Effect of Antarctic Sea Ice on Southern Ocean Carbon Outgassing: Capping versus Light Attenuation. *Global Biogeochemical Cycles*, *n/a*(n/a), e2019GB006489. Retrieved from https://agupubs.onlinelibrary.wiley.com/doi/abs/10.1029/2019GB006489 doi: 10.1029/2019GB006489

Hallberg, R., & Gnanadesikan, A. (2006). The role of eddies in determining the structure and response of the wind-driven southern hemisphere overturning: Results from the Modeling Eddies in the Southern Ocean (MESO) project. *Journal of physical oceanography*, *36*(12), 2232–2252.

Hauck, J., Gregor, L., Nissen, C., Patara, L., Hague, M., Mongwe, P., ... Séférian, R. (2022, may). Characterizing the Southern Ocean Carbon Sink 1985 to 2018: A Synthesis in the Framework of the RECCAP2 Project. In *Royal society meeting.* https://royalsociety.org/science-events-and-lectures/2022/05/southern-ocean/. Retrieved from https://royalsociety.org/science-events-and-lectures/2022/05/southern-ocean/

Hauck, J., Völker, C., Wang, T., Hoppema, M., Losch, M., & Wolf-Gladrow, D. A. (2013). Seasonally different carbon flux changes in the Southern Ocean in response to the southern annular mode. *Global Biogeochemical Cycles*, *27*(4), 1236–1245. Retrieved from https://agupubs.onlinelibrary.wiley.com/doi/abs/10.1002/2013GB004600 doi: https://doi.org/10.1002/2013GB004600

Hauck, J., Zeising, M., Le Quéré, C., Gruber, N., Bakker, D. C. E., Bopp, L., ... Séférian, R. (2020). Consistency and Challenges in the Ocean Carbon Sink Estimate for the Global Carbon Budget. *Frontiers in Marine Science*, *7*. Retrieved from https://www.frontiersin.org/articles/10.3389/fmars.2020.571720 doi: 10.3389/fmars.2020.571720

Hersbach, H., Bell, B., Berrisford, P., Hirahara, S., Horányi, A., Muñoz-Sabater, J., ... Thépaut, J.-N. (2020). The ERA5 global reanalysis. *Quarterly Journal of the Royal Meteorological Society*, *146*(730), 1999–2049. Retrieved from https://rmets.onlinelibrary.wiley.com/doi/abs/10.1002/qj.3803 doi:

https://doi.org/10.1002/qj.3803

Holte, J., & Talley, L. (2009). A New Algorithm for Finding Mixed Layer Depths with Applications to Argo Data and Subantarctic Mode Water Formation. *Journal of Atmospheric and Oceanic Technology*, *26*(9), 1920–1939. Retrieved from `https://doi.org/10.1175/2009JTECHO543.1` doi: 10.1175/2009JTECHO543.1

Humphreys, M. P., Schiller, A. J., Sandborn, D. E., Gregor, L., Pierrot, D., van Heuven, S. M. A. C., ... Wallace, D. W. R. (2021). *PyCO2SYS: marine carbonate system calculations in Python.* Zenodo. doi: doi:10.5281/zenodo.3744275.

Ito, T., Woloszyn, M., & Mazloff, M. (2010). Anthropogenic carbon dioxide transport in the Southern Ocean driven by Ekman flow. *Nature*, *463*(7277), 80–83. Retrieved from `https://doi.org/10.1038/nature08687` doi: 10.1038/nature08687

Johnson, K. S., Plant, J. N., Coletti, L. J., Jannasch, H. W., Sakamoto, C. M., Riser, S. C., ... Sarmiento, J. L. (2017). Biogeochemical sensor performance in the SOCCOM profiling float array. *Journal of Geophysical Research: Oceans*, *122*(8), 6416–6436. Retrieved from `https://agupubs.onlinelibrary.wiley.com/doi/abs/10.1002/2017JC012838` doi: https://doi.org/10.1002/2017JC012838

Jouandet, M. P., Blain, S., Metzl, N., Brunet, C., Trull, T. W., & Obernosterer, I. (2008). A seasonal carbon budget for a naturally iron-fertilized bloom over the Kerguelen Plateau in the Southern Ocean. *Deep Sea Research Part II: Topical Studies in Oceanography*, *55*(5), 856–867. Retrieved from `https://www.sciencedirect.com/science/article/pii/S0967064508000209` doi: https://doi.org/10.1016/j.dsr2.2007.12.037

Krumhardt, K. M., Long, M. C., Lindsay, K., & Levy, M. N. (2020). Southern Ocean Calcification Controls the Global Distribution of Alkalinity. *Global Biogeochemical Cycles*, *34*(12), e2020GB006727. Retrieved from `https://agupubs.onlinelibrary.wiley.com/doi/abs/10.1029/2020GB006727` doi: https://doi.org/10.1029/2020GB006727

Landschützer, P., Gruber, N., Bakker, D. C. E., & Schuster, U. (2014). Recent variability of the global ocean carbon sink. *Global Biogeochemical Cycles*, *28*(9), 927–949. Retrieved from `https://agupubs.onlinelibrary.wiley.com/doi/abs/10.1002/2014GB004853` doi: https://doi.org/10.1002/2014GB004853

Law, C. S., Abraham, E. R., Watson, A. J., & Liddicoat, M. I. (2003). Vertical eddy diffusion and nutrient supply to the surface mixed layer of the Antarctic Circumpolar Current. *Journal of Geophysical Research C: Oceans*, *108*(8), 28–1. doi: 10.1029/2002JC001604

Lee, K., Kim, T.-W., Byrne, R. H., Millero, F. J., Feely, R. A., & Liu, Y.-M. (2010). The universal ratio of boron to chlorinity for the North Pacific and North Atlantic oceans. *Geochimica et Cosmochimica Acta*, *74*(6), 1801–1811. Retrieved from `https://www.sciencedirect.com/science/article/pii/S0016703709007789` doi: https://doi.org/10.1016/j.gca.2009.12.027

Levy, M., Bopp, L., Karleskind, P., Resplandy, L., Ethe, C., & Pinsard, F. (2013, dec). Physical pathways for carbon transfers between the surface mixed layer and the ocean interior [Article]. *GLOBAL BIOGEOCHEMICAL CYCLES*, *27*(4), 1001–1012. doi: 10.1002/gbc.20092

Li, H., Xie, H., Kern, S., Wan, W., Ozsoy, B., Ackley, S., & Hong, Y. (2018). Spatio-temporal variability of Antarctic sea-ice thickness and volume obtained from ICESat data using an innovative algorithm. *Remote Sensing of Environment*, *219*, 44–61. Retrieved from `http://www.sciencedirect.com/science/article/pii/S0034425718304425` doi: https://doi.org/10.1016/j.rse.2018.09.031

Long, M. C., Stephens, B. B., McKain, K., Sweeney, C., Keeling, R. F., Kort,

E. A., ... Wofsy, S. C. (2021). Strong Southern Ocean carbon uptake evident in airborne observations. *Science*, *374*(6572), 1275–1280. Retrieved from https://www.science.org/doi/abs/10.1126/science.abi4355 doi: 10.1126/science.abi4355

Lueker, T. J., Dickson, A. G., & Keeling, C. D. (2000). Ocean pCO2 calculated from dissolved inorganic carbon, alkalinity, and equations for K1 and K2: validation based on laboratory measurements of CO2 in gas and seawater at equilibrium. *Marine Chemistry*, *70*(1), 105–119. Retrieved from https://www.sciencedirect.com/science/article/pii/S0304420300000220 doi: https://doi.org/10.1016/S0304-4203(00)00022-0

MacGilchrist, G. A., Naveira Garabato, A. C., Brown, P. J., Jullion, L., Bacon, S., Bakker, D. C., ... Torres-Valdés, S. (2019). Reframing the carbon cycle of the subpolar Southern Ocean. *Science Advances*, *5*(8), 1–8. doi: 10.1126/sciadv.aav6410

Maurer, T. L., Plant, J. N., & Johnson, K. S. (2021). Delayed-Mode Quality Control of Oxygen, Nitrate, and pH Data on SOCCOM Biogeochemical Profiling Floats. *Frontiers in Marine Science*, *8*, 1118. Retrieved from https://www.frontiersin.org/article/10.3389/fmars.2021.683207 doi: 10.3389/fmars.2021.683207

McDougall, T., & Barker, P. (2011). Getting started with TEOS-10 and the Gibbs Seawater (GSW) Oceanographic Toolbox. , *SCOR/IAPSO*(WG127), 28. doi: 978-0-646-55621-5

McNeil, B. I., & Tilbrook, B. (2009). A seasonal carbon budget for the sub-Antarctic Ocean, South of Australia. *Marine Chemistry*, *115*(3), 196–210. Retrieved from https://www.sciencedirect.com/science/article/pii/S0304420309001212 doi: https://doi.org/10.1016/j.marchem.2009.08.006

Merlivat, L., Boutin, J., & Antoine, D. (2015, jul). Roles of biological and physical processes in driving seasonal air-sea CO2 flux in the Southern Ocean: New insights from CARIOCA pCO(2) [Article]. *JOURNAL OF MARINE SYSTEMS*, *147*(SI), 9–20. doi: 10.1016/j.jmarsys.2014.04.015

Mongwe, N. P., Vichi, M., & Monteiro, P. M. S. (2018). The seasonal cycle of pCO$_{2}$ and CO$_{2}$ fluxes in the Southern Ocean: diagnosing anomalies in CMIP5 Earth system models. *Biogeosciences*, *15*(9), 2851–2872. Retrieved from https://bg.copernicus.org/articles/15/2851/2018/ doi: 10.5194/bg-15-2851-2018

Orsi, A. H., Whitworth, T., & Nowlin, W. D. (1995). On the meridional extent and fronts of the Antarctic Circumpolar Current. *Deep Sea Research Part I: Oceanographic Research Papers*, *42*(5), 641–673. Retrieved from http://www.sciencedirect.com/science/article/pii/096706379500021W doi: https://doi.org/10.1016/0967-0637(95)00021-W

Perez, F. F., & Fraga, F. (1987). Association constant of fluoride and hydrogen ions in seawater. *Marine Chemistry*, *21*(2), 161–168. Retrieved from https://www.sciencedirect.com/science/article/pii/0304420387900363 doi: https://doi.org/10.1016/0304-4203(87)90036-3

Prend, C. J., Hunt, J. M., Mazloff, M. R., Gille, S. T., & Talley, L. D. (2022). Controls on the Boundary Between Thermally and Non-Thermally Driven pCO2 Regimes in the South Pacific. *Geophysical Research Letters*, *49*(9), e2021GL095797. Retrieved from https://agupubs.onlinelibrary.wiley.com/doi/abs/10.1029/2021GL095797 doi: https://doi.org/10.1029/2021GL095797

Roemmich, D., & Gilson, J. (2009). The 2004–2008 mean and annual cycle of temperature, salinity, and steric height in the global ocean from the Argo Program. *Progress in Oceanography*, *82*(2), 81–100. Retrieved from https://www.sciencedirect.com/science/article/pii/S0079661109000160 doi: https://doi.org/10.1016/j.pocean.2009.03.004

Rosso, I., Mazloff, M. R., Verdy, A., & Talley, L. D. (2017). Space and time variability of the Southern Ocean carbon budget. *Journal of Geophysical Research: Oceans*, *122*(9), 7407–7432. Retrieved from https://agupubs.onlinelibrary.wiley.com/doi/abs/10.1002/2016JC012646 doi: https://doi.org/10.1002/2016JC012646

Saenz, B. T., & Arrigo, K. R. (2014). Annual primary production in Antarctic sea ice during 2005–2006 from a sea ice state estimate. *Journal of Geophysical Research: Oceans*, *119*(6), 3645–3678. Retrieved from https://agupubs.onlinelibrary.wiley.com/doi/abs/10.1002/2013JC009677 doi: https://doi.org/10.1002/2013JC009677

Shadwick, E. H., De Meo, O. A., Schroeter, S., Arroyo, M. C., Martinson, D. G., & Ducklow, H. (2021). Sea Ice Suppression of CO2 Outgassing in the West Antarctic Peninsula: Implications For The Evolving Southern Ocean Carbon Sink. *Geophysical Research Letters*, *48*(11), e2020GL091835. Retrieved from https://agupubs.onlinelibrary.wiley.com/doi/abs/10.1029/2020GL091835 doi: https://doi.org/10.1029/2020GL091835

Shadwick, E. H., Trull, T. W., Tilbrook, B., Sutton, A. J., Schulz, E., Trull, T. W., ... Sabine, C. L. (2015). Seasonality of biological and physical controls on surface ocean CO 2 from hourly observations at the Southern Ocean Time Series site south of Australia. *Global biogeochemical cycles.*, *29*(2), 223–238.

Takahashi, T., Feely, R. A., Weiss, R. F., Wanninkhof, R. H., Chipman, D. W., Sutherland, S. C., & Takahashi, T. T. (1997). Global air-sea flux of CO2: An estimate based on measurements of sea–air pCO2 difference. *Proceedings of the National Academy of Sciences*, *94*(16), 8292–8299. Retrieved from https://www.pnas.org/doi/abs/10.1073/pnas.94.16.8292 doi: 10.1073/pnas.94.16.8292

Takahashi, T., Olafsson, J., Goddard, J. G., Chipman, D. W., & Sutherland, S. C. (1993). Seasonal variation of CO2 and nutrients in the high-latitude surface oceans: A comparative study. *Global Biogeochemical Cycles*, *7*(4), 843–878. Retrieved from https://agupubs.onlinelibrary.wiley.com/doi/abs/10.1029/93GB02263 doi: https://doi.org/10.1029/93GB02263

Takahashi, T., Sutherland, S. C., Sweeney, C., Poisson, A., Metzl, N., Tilbrook, B., ... Nojiri, Y. (2002). Global sea–air CO2 flux based on climatological surface ocean pCO2, and seasonal biological and temperature effects. *Deep Sea Research Part II: Topical Studies in Oceanography*, *49*(9), 1601–1622. Retrieved from https://www.sciencedirect.com/science/article/pii/S0967064502000036 doi: https://doi.org/10.1016/S0967-0645(02)00003-6

Takahashi, T., Sutherland, S. C., Wanninkhof, R., Sweeney, C., Feely, R. A., Chipman, D. W., ... de Baar, H. J. W. (2009). Climatological mean and decadal change in surface ocean pCO2, and net sea–air CO2 flux over the global oceans. *Deep Sea Research Part II: Topical Studies in Oceanography*, *56*(8), 554–577. Retrieved from https://www.sciencedirect.com/science/article/pii/S0967064508004311 doi: https://doi.org/10.1016/j.dsr2.2008.12.009

Vihma, T., & Haapala, J. (2009). Geophysics of sea ice in the Baltic Sea: A review. *Progress in Oceanography*, *80*(3), 129–148. Retrieved from https://www.sciencedirect.com/science/article/pii/S0079661109000123 doi: https://doi.org/10.1016/j.pocean.2009.02.002

Wanninkhof, R., Johnson, K., Williams, N., Sarmiento, J., Riser, S., Briggs, E., ... Verdy, A. (2016). *An evaluation of pH and NO3 sensor data from SOCCOM floats and their utilization to develop ocean inorganic carbon products* (Tech. Rep.). Retrieved from https://soccom.princeton.edu/sites/default/files/files/CWG{_}white{_}paper{_}March{_}13{_}2016.pdf

Williams, N. L., Juranek, L. W., Feely, R. A., Russell, J. L., Johnson, K. S., & Hales, B. (2018). Assessment of the Carbonate Chemistry Seasonal Cycles in the Southern Ocean From Persistent Observational Platforms. *Journal of Geophysical Research: Oceans*, *123*(7), 4833–4852. Retrieved from `https://agupubs.onlinelibrary.wiley.com/doi/abs/10.1029/2017JC012917` doi: https://doi.org/10.1029/2017JC012917

Wong, A. P. S., Wijffels, S. E., Riser, S. C., Pouliquen, S., Hosoda, S., Roemmich, D., ... Park, H.-M. (2020). Argo Data 1999–2019: Two Million Temperature-Salinity Profiles and Subsurface Velocity Observations From a Global Array of Profiling Floats. *Frontiers in Marine Science*, *7*, 700. Retrieved from `https://www.frontiersin.org/article/10.3389/fmars.2020.00700` doi: 10.3389/fmars.2020.00700

Yang, B., Shadwick, E. H., Schultz, C., & Doney, S. C. (2021). Annual Mixed Layer Carbon Budget for the West Antarctic Peninsula Continental Shelf: Insights From Year-Round Mooring Measurements. *Journal of Geophysical Research: Oceans*, *126*(4), e2020JC016920. Retrieved from `https://agupubs.onlinelibrary.wiley.com/doi/abs/10.1029/2020JC016920` doi: https://doi.org/10.1029/2020JC016920